

1 **Tropopause Evolution in a Rapidly Intensifying Tropical Cyclone: A Static**
2 **Stability Budget Analysis in an Idealized, Axisymmetric Framework**

3 Patrick Duran* and John Molinari

4 *University at Albany, State University of New York, Albany, NY*

5 **Corresponding author address:* Department of Atmospheric and Environmental Sciences, Univer-
6 sity at Albany, State University of New York, 1400 Washington Avenue, Albany, NY.

7 E-mail: pduran2008@gmail.com

ABSTRACT

8 Large changes in tropopause-layer static stability are observed during the
9 rapid intensification (RI) of an idealized, axisymmetric tropical cyclone (TC).
10 Over the eye, static stability near the tropopause decreases and the cold-point
11 tropopause height rises by up to 4 km at the storm center. Outside of the eye,
12 static stability immediately above the cold-point tropopause increases consid-
13 erably, and the tropopause remains near its initial level. A budget analysis
14 reveals that advection contributes to the static stability tendencies at all times
15 throughout the upper troposphere and lower stratosphere. Advection is partic-
16 ularly important within the eye, where it acts to destabilize the layer near and
17 above the cold-point tropopause. Outside of the eye, a radial-vertical circula-
18 tion develops during RI, with strong outflow below the tropopause and weak
19 inflow above. Vertical wind shear above and below the upper-tropospheric
20 outflow maximum induces turbulence, which provides forcing for both desta-
21 bilization and stabilization in the tropopause layer. Meanwhile, as organized
22 convection reaches the tropopause, radiative heating tendencies at the top of
23 the cirrus canopy generally act to destabilize the upper troposphere and stabi-
24 lize the lower stratosphere. Turbulent mixing and radiative heating combine
25 to play an important role in the development of the strong stable layer im-
26 mediately above the cold-point tropopause during RI. The results suggest that
27 turbulence and radiation, alongside advection, play fundamental roles in the
28 upper-level static stability evolution of TCs.

29 **1. Introduction**

30 After undergoing a remarkably rapid intensification (RI), Hurricane Patricia (2015) set a new
31 record as the strongest tropical cyclone (TC) ever observed in the Western Hemisphere (Kim-
32 berlain et al. 2016; Rogers et al. 2017). High-altitude dropsonde observations taken during the
33 Tropical Cyclone Intensity (TCI) experiment captured this RI in unprecedented detail (Doyle et al.
34 2017). These observations revealed dramatic changes in the structure of the cold-point tropopause
35 and upper-level static stability as the storm intensified (Duran and Molinari 2018).

36 At tropical storm intensity, shortly before RI commenced, a strong inversion layer existed just
37 above Patricia’s cold-point tropopause, which was located near 17.2 km. During the first half of
38 the RI period, this inversion layer weakened throughout Patricia’s inner core, with the weakening
39 most pronounced over the developing eye. By the time the storm reached its maximum intensity,
40 the inversion layer over the eye had disappeared almost completely, which was accompanied by an
41 increase in the tropopause height to a level at or above the highest-available dropsonde data point
42 (18.3 km) at two locations. Meanwhile over the eyewall region, the static stability re-strengthened
43 and the tropopause was limited to a level at or below 17.5 km. The mechanisms that led to these
44 changes in upper-level static stability and tropopause height are the subject of the current paper.

45 Despite the importance of tropopause-layer thermodynamics in theoretical models of hurricanes
46 (Emanuel and Rotunno 2011; Emanuel 2012), few papers have examined the upper-tropospheric
47 evolution of TCs. Komaromi and Doyle (2017) found that stronger TCs tended to have a higher
48 and warmer tropopause over their inner core than weaker TCs. Their results are consistent with
49 the evolution observed over the inner core of Hurricane Patricia, in which the tropopause height
50 increased and the tropopause temperature warmed throughout RI (Duran and Molinari 2018).

51 Idealized simulations of a TC analyzed by Ohno and Satoh (2015) suggested that the develop-
 52 ment of an upper-level warm core near the TC storm center acted to decrease the static stability
 53 near the tropopause (see their Fig.). Although the mechanisms that drive this static stability
 54 evolution have not been examined explicitly, Stern and Zhang (2013) described the development
 55 of the TC warm core using a potential temperature (θ) budget analysis. They found that radial
 56 and vertical advection both played important roles in warm core development throughout RI, and
 57 subgrid-scale diffusion became particularly important during the later stage of RI. To our knowl-
 58 edge, the only paper that has examined explicitly the static stability evolution in a modeled TC is
 59 Kepert et al. (2016), but their analysis was limited to the boundary layer. The analysis herein is
 60 based upon that of Stern and Zhang (2013), except using a static stability budget similar to that of
 61 Kepert et al. (2016), with a focus on the upper troposphere and lower stratosphere.

62 **2. Model Setup**

63 The numerical simulations were performed using version 19.4 of Cloud Model 1 (CM1) de-
 64 scribed in Bryan and Rotunno (2009). The equations of motion were integrated on a 3000-km-
 65 wide, 30-km-deep axisymmetric grid with 1-km horizontal and 250-m vertical grid spacing. The
 66 computations were performed on an f -plane at 15°N latitude, over a sea surface with constant
 67 temperature of 30.5°C, which matches that observed near Hurricane Patricia (2015; Kimberlain
 68 et al. 2016). Horizontal turbulence was parameterized using the Smagorinsky scheme described in
 69 Bryan and Rotunno (2009, pg. 1773), with a prescribed mixing length that varied linearly from 100
 70 m at a surface pressure of 1015 hPa to 1000 m at a surface pressure of 900 hPa. This formulation
 71 allows for realistically-large horizontal mixing lengths near the hurricane’s inner core, consistent
 72 with the results of Bryan (2012), while not over-representing horizontal turbulence in convection
 73 at outer radii. Vertical turbulence was parameterized using the formulation of Markowski and

74 Bryan (2016, their Eq. 6), using an asymptotic vertical mixing length of 100 m. A Rayleigh
75 damping layer was applied outside of the 2900-km radius and above the 25-km level to prevent
76 spurious gravity wave reflection at the model boundaries. Microphysical processes were param-
77 eterized using the Thompson et al. (2004) microphysics scheme and radiative heating tendencies
78 were computed every two minutes using the Rapid Radiative Transfer Model for GCMs (RRTMG)
79 longwave and shortwave schemes (Iacono et al. 2008). The initial temperature and humidity field
80 was horizontally homogeneous and determined by averaging all Climate Forecast System Reanal-
81 ysis (CFSR) grid points within 100 km of Patricia's center of circulation at 18 UTC 21 October
82 2015. The vortex described in Rotunno and Emanuel (1987, their Eq. 37) was used to initialize
83 the wind field, setting all parameters equal to the values used therein.

84 Although hurricanes simulated in an axisymmetric framework tend to be more intense than
85 those observed in nature, the intensity evolution of this simulation matches reasonably well with
86 that observed in Hurricane Patricia. After an initial spin-up period of about 20 hours, the modeled
87 storm (Fig.1, blue lines) began an RI period that lasted approximately 30 hours. After this RI, the
88 storm continued to intensify more slowly until the maximum 10-m wind speed reached 89 m s^{-1}
89 and the minimum sea-level pressure reached its minimum of 846 mb, 81 hours into the simulation.
90 Hurricane Patricia (red stars) exhibited a similar intensity evolution, with an RI period leading to a
91 maximum 10-m wind speed of 95 m s^{-1} and a minimum sea-level pressure of 872 hPa. Despite the
92 limitations of the axisymmetric framework, the extraordinary intensity of Hurricane Patricia and
93 the rapidity of its intensification makes Patricia a particularly good candidate for axisymmetric
94 analysis.

95 3. Budget Computation

96 The static stability can be expressed as the squared Brunt Väisälä frequency:

$$N_m^2 = \frac{g}{T} \left(\frac{\partial T}{\partial z} + \Gamma_m \right) \left(1 + \frac{T}{R_d/R_v + q_s} \frac{\partial q_s}{\partial T} \right) - \frac{g}{1 + q_t} \frac{\partial q_t}{\partial z}, \quad (1)$$

97 where g is gravitational acceleration, T is temperature, R_d and R_v are the gas constants of dry air
 98 and water vapor, respectively, q_s is the saturation mixing ratio, q_t is the total condensate mixing
 99 ratio, and Γ_m is the moist-adiabatic lapse rate:

$$\Gamma_m = g(1 + q_t) \left(\frac{1 + L_v q_s / R_d T}{c_{pm} + L_v \partial q_s / \partial T} \right), \quad (2)$$

100 where L_v is the latent heat of vaporization and c_{pm} is the specific heat of moist air at constant
 101 pressure. In the tropopause layer, q_s , $\partial q_s / \partial T$, and $\partial q_t / \partial z$ approach zero. In this limiting case,
 102 Eq. 1 reduces to:

$$N^2 = \frac{g}{\theta} \frac{\partial \theta}{\partial z}, \quad (3)$$

103 where θ is the potential temperature.

104 To compute N^2 , CM1 uses Eq.1 in saturated environments and Eq. 3 in sub-saturated environ-
 105 ments. For simplicity, however, only Eq. 3 will be employed for the budget computations herein¹.

106 Taking the time derivative of Eq. 3 yields the static stability tendency:

$$\frac{\partial N^2}{\partial t} = \frac{g}{\theta} \frac{\partial}{\partial z} \frac{\partial \theta}{\partial t} - \frac{g}{\theta^2} \frac{\partial \theta}{\partial z} \frac{\partial \theta}{\partial t}, \quad (4)$$

107 where the potential temperature tendency, $\partial \theta / \partial t$, can be written:

$$\frac{\partial \theta}{\partial t} = HADV + VADV + HTURB + VTURB + MP + RAD + DISS \quad (5)$$

108 Each term on the right-hand side of Eq. 5 represents a θ budget variable, each of which is out-
 109 put directly by the model every minute. HADV and VADV are the radial and vertical advective

¹The validity of this approximation will be substantiated later in this section.

tendencies², HTURB and VTURB are the radial and vertical tendencies from the turbulence parameterization, MP is the tendency from the microphysics scheme, RAD is the tendency from the radiation scheme, and DISS is the tendency due to turbulent dissipation. This equation neglects Rayleigh damping, since this term is zero everywhere below 25 km, and the analysis domain does not extend to that level. Each term in Eq. 5 is substituted for $\partial\theta/\partial t$ in Eq. 4, yielding the contribution of each budget term to the static stability tendency. These terms are summed, yielding an instantaneous "budget change" in N^2 every minute. The budget changes are then averaged over 24-hour periods and compared to the total model change in N^2 over that same time period, i.e.:

$$\Delta N_{budget}^2 = \frac{1}{\delta t} \sum_{t=t_0}^{t_0+\delta t} \left. \frac{\partial N^2}{\partial t} \right|_t \quad (6)$$

$$\Delta N_{model}^2 = N_{t_0+\delta t}^2 - N_{t_0}^2 \quad (7)$$

$$Residual = \Delta N_{model}^2 - \Delta N_{budget}^2 \quad (8)$$

where t_0 is an initial time and δt is 24 hours.

Eqs. 6-8 are plotted for four consecutive 24-hour periods in Fig. 2. For this and all subsequent radial-vertical cross sections, a 1-2-1 smoother is applied once in the radial direction to eliminate $2\Delta r$ noise that appears in some of the raw model output and calculated fields. The left column of Fig. 2 depicts the model changes (Eq. 7), the center column depicts the budget changes (Eq. 6), and the right column depicts the residuals (Eq. 8). In every 24-hour period, the budget changes are nearly identical to the model changes, which is reflected in the near-zero residuals in the right column. This indicates that the budget accurately represents the model variability, which implies that the neglect of moisture in the budget computation introduces negligible error within the analysis domain³.

²These terms include the tendencies due to the diffusion that is implicit in the fifth-order advection scheme.

³This is not the case in the lower- and mid-troposphere, where the residual actually exceeds the budget variability in many places, likely due to the neglect of moisture; thus we limit this analysis to the upper troposphere and lower stratosphere.

130 In the tropopause layer, some of the budget terms are small enough to be ignored. To determine
 131 which of the budget terms are most important, a time series of the contribution of each of the
 132 budget terms in Eq. 5 to the tropopause-layer static stability tendency is plotted in Fig. 4. For this
 133 figure, each of the budget terms is computed using the method described in Section 3, except with
 134 1-hour averaging intervals instead of 24-hour intervals. The absolute values of these tendencies
 135 are then averaged over a radius-height domain surrounding the tropopause and plotted as a time
 136 series⁴. Advection (Fig. 4, red line) plays an important role in the mean tropopause-layer static
 137 stability tendency at all times, and vertical turbulence (Fig. 4, blue line) and radiation (Fig. 4, dark
 138 green line) also contribute significantly. Although the contribution from horizontal turbulence
 139 (Fig. 4, purple line) becomes more important after 48 hours, it is confined to a very small region
 140 immediately surrounding the eyewall tangential velocity maximum (not shown), and is negligible
 141 throughout the rest of the tropopause layer. The remaining two processes - microphysics and
 142 dissipative heating (Fig. 4, orange and light green lines, respectively) - lie atop one another near
 143 zero. These time series indicate that, at all times, three budget terms dominate the tropopause-layer
 144 static stability tendency: advection, vertical turbulence, and radiation. Variations in the magnitude
 145 and spatial structure of these terms drive the static stability changes depicted in Fig. 2; subsequent
 146 sections will focus on these variations and what causes them.

⁴It will be seen in subsequent figures that each of the terms contributes both positively and negatively to the N^2 tendency within the analysis domain. Thus, taking an average over the domain tends to wash out the positive and negative contributions. To circumvent this problem, the absolute value of each of the terms is averaged.

4. Results

a. Static stability evolution

The average N^2 over the first day of the simulation (Fig. 3a) indicates the presence of a weak static stability maximum just above the cold-point tropopause. Over the subsequent 24 hours, during the RI period, the static stability within and above this layer decreased near the storm center (Fig. 3b). This decreasing N^2 corresponded to an increase in the tropopause height within the developing eye, maximized at the storm center. Outside of the eye, meanwhile, the tropopause height decreased over the eyewall region (25-60-km radius) and increased only slightly outside of the 60-km radius. In this outer region, the N^2 maximum just above the tropopause strengthened during RI. These trends continued as the storm's intensity leveled off in the 48-72-hour period (Fig. 3c). The tropopause height increased to nearly 21 km at the storm center and sloped sharply downward to 16.3 km on the inner edge of the eyewall, near the 30 km radius. Static stability outside of the eye, meanwhile, continued to increase just above the cold-point tropopause. This N^2 evolution closely follows that observed in Hurricane Patricia (2015; Duran and Molinari 2018). The mechanisms that led to these static stability changes will be investigated in the subsequent sections.

b. Static stability budget analysis

(i) 0-24 hours The weakening of the lower-stratospheric static stability maximum during the initial spin-up period is reflected in the total N^2 budget change over this time (Fig. 5a). The 17-18-km layer was characterized by decreasing N^2 (purple shading), maximizing at the storm center. The layer immediately below the tropopause, meanwhile, saw strengthening N^2 during this time period. Although these tendencies extended out to the 200-km radius, they were particularly

pronounced at innermost radii. A comparison of the contributions of advection (Fig. 5b), vertical turbulence (Fig. 5c), and radiation (Fig. 5d) reveals that advection is primarily responsible for the change in static stability during this period. Although vertical turbulence acts in opposition to advection (i.e. it acts to stabilize regions that advection acts to destabilize), the magnitude of the advective tendencies is larger, particularly at the innermost radii. The sum of advection and vertical turbulence (Fig. 5e) almost exactly replicates the static stability tendencies above 17 km. Radiative tendencies (Fig. 5d) act to destabilize the layer below about 16 km and stabilize the layer between 16 and 17 km. The sum of advection, vertical turbulence, and radiation (Fig. 5f) reproduces the total change in N^2 almost exactly.

...Explain this in the context of radial and vertical velocities... ...See Stern and Zhang, Page 84, Section 3d... ...Add mention of total condensate and radiative heating tendencies as it relates to stability tendency due to rad...

(ii) *24-48 hours* During the RI period, N^2 within the eye generally decreased above 16 km and increased below (Fig. 6a). These tendencies at the innermost radii were driven almost entirely by advection (Fig. 6b); vertical turbulence (Fig. 6c) and radiation (Fig. 6d) contributed negligibly to the static stability tendencies in this region.

Outside of the eye, the N^2 evolution exhibited alternating layers of positive and negative tendencies. Near and above 18 km existed an upward-sloping region of decreasing N^2 that extended out to the 180-km radius. In this region, neither vertical turbulence nor radiation exhibited negative N^2 tendencies; advection was the only forcing for destabilization. Immediately below this layer was a region of increasing N^2 , which sloped upward from 17 km near the 30-km radius to just below 18 km outside of the 100-km radius. Advection and vertical turbulence both contributed to this positive N^2 tendency, with advection playing an important role below about 17.5 km and and

192 turbulence playing an important role above. The sum of advection and turbulence (Fig. 6e) reveals
 193 two discontinuous regions of increasing N^2 in the 17-18-km layer rather than one contiguous re-
 194 gion. The addition of radiation to these two terms, however, (Fig. 6f) provides the link between
 195 these two regions, indicating that radiation also plays a role in strengthening the stable layer just
 196 above the tropopause. In the 16-17-km layer, a horizontally-extensive layer of decreasing N^2 also
 197 was forced by a combination of advection, vertical turbulence, and radiation. The sum of advec-
 198 tion and vertical turbulence accounts for only a portion of the decreasing N^2 in this layer, and
 199 actually indicates forcing for stabilization near the 50-km radius and outside of the 130-km radius.
 200 Radiative tendencies overcome this forcing for stabilization in both of these regions to produce the
 201 radially-extensive region of destabilization observed just below the tropopause.

202 TWO REGIONS WHERE Panel (f) differs from panel (a): 30-60 km radial band below 16 km,
 203 which is actually canceled out by a vertical gradient of latent heating, and the thin region of strong
 204 stabilization between 15-17.5 km near $r=30$ km, which is canceled out by horizontal turbulence.

205 (iii) 48-72 hours After the storm's maximum wind speed leveled off near 80 m s^{-1} , the magnitude
 206 of the static stability tendencies within the eye decreased to near zero (Fig. 7a).

207 Outside of the eye, however, N^2 continued to increase just above the tropopause and decrease
 208 just below. The sum of advection and vertical turbulence (Fig. 7e) indicates that the increase of
 209 N^2 observed in the 17-18-km layer and inside of the 80-km radius cannot be attributed to these
 210 processes, since the sum of these two terms provided forcing for destabilization. Instead, radiation
 211 (Fig. 7d), provided the forcing for stabilization in this region. Outside of the 80-km radius, both
 212 advection (Fig. 7b) and vertical turbulence (Fig. 7c) provided forcing for stabilization near the
 213 18-km level. The sum of the two terms indicates increasing N^2 near the 18-km level everywhere
 214 outside of the 80-km radius, but this stabilization is slightly weaker in the 90-120-km radial band

215 than the observed value. The addition of radiation (Fig. 7f) provides the extra forcing for stabi-
 216 lization required to account for the observed increase in N^2 . Outside of the 120-km radius, the
 217 region of radiative forcing for stabilization slopes downward, and the increase in N^2 observed near
 218 18 km can be explained entirely by a combination of advection and vertical turbulence. The layer
 219 of decreasing N^2 observed near 17 km was forced primarily by vertical turbulence and radiation.
 220 Within most of this region, advection provided strong forcing for stabilization, but this forcing
 221 was outweighed by the negative N^2 tendencies induced by a combination of vertical turbulence
 222 and radiation.

223 5. Discussion

224 a. *The role of advection*

225 Advection played an important role in the tropopause-layer N^2 evolution at all stages of intensi-
 226 fication, but for brevity, this section will focus only on the RI (24-48-hour) period. To investigate
 227 the advective processes more closely, the individual contributions of horizontal and vertical advec-
 228 tion during the RI period are shown in Fig. 8, along with the corresponding time-mean radial and
 229 vertical velocities and θ . The N^2 tendencies due to the two advective components (Fig. 8a,b) ex-
 230 hibit strong cancellation, consistent with flow that is nearly isentropic. There are, however, some
 231 regions in which flow crosses θ surfaces; this flow accounts for all non-zero N^2 tendencies due to
 232 advection previously seen in Fig. 6b.

233 Some insight can be gained by considering the time tendency of the vertical θ gradient due to
 234 advection:

$$\left(\frac{\partial}{\partial t} \frac{\partial \theta}{\partial z} \right)_{adv} = -u \frac{\partial}{\partial r} \frac{\partial \theta}{\partial z} - w \frac{\partial}{\partial z} \frac{\partial \theta}{\partial z} - \frac{\partial u}{\partial z} \frac{\partial \theta}{\partial r} - \frac{\partial w}{\partial z} \frac{\partial \theta}{\partial z}. \quad (9)$$

235 The first two terms on the right-hand side of Eq. 9 represent advection of static stability by
 236 the radial and vertical wind, respectively. These terms cannot create a maximum or a minimum;
 237 they only act to rearrange the static stability field. Since the goal of this analysis is to understand
 238 the processes responsible for the creation of maxima and minima in N^2 , these two terms will not
 239 be examined. The third and fourth terms represent, respectively, the tilting of isentropes in the
 240 presence of vertical wind shear, and the spreading or compaction of isentropes through divergence
 241 of the vertical wind. Since these terms involve gradients of velocities, they can create or eliminate
 242 local maxima or minima in static stability. This section will focus on these two terms.

243 During the RI period, strong radial and vertical circulations developed near the tropopause,
 244 which forced high-magnitude N^2 tendencies due to advection (Fig. 8a,b). A layer of strong outflow
 245 developed at and below the tropopause during this period, with the outflow maximum (dashed cyan
 246 line) curving from the 14-km level at the 50-km radius to just below the 16-km level outside of
 247 the 80-km radius (Fig. 8c). The cyan line, by definition, represents the level at which the vertical
 248 gradient of radial velocity switched signs, with $\partial u / \partial z > 0$ below the line and $\partial u / \partial z < 0$ above.
 249 Notably, the N^2 tendency due to horizontal advection (Fig. 8a) also tended to switch signs very
 250 near this line, with stabilization below the outflow maximum and destabilization above. This
 251 suggests that vertical wind shear above and below the outflow maximum played an important
 252 role in the N^2 tendency during this time. Examination of the third term on the right-hand side
 253 of Eq. 9 reveals that tilting of isentropes within these shear layers contributed to the strong N^2
 254 tendencies that flanked the outflow maximum. Outside of the eye and eyewall, isentropes generally
 255 sloped upward with radius, which means that θ decreased outward ($\partial \theta / \partial r < 0$). Thus, wherever
 256 $\partial u / \partial z > 0$, the tilting term must force an increase in N^2 , and wherever $\partial u / \partial z < 0$, the tilting term
 257 must force a decrease in N^2 . This is precisely the structure seen in Fig. 8a, which suggests that the
 258 tilting term might be important near the outflow jet.

Advection of N^2 by the radial wind (first term on the right-hand side of Eq. 9) also acts within the outflow jet. For example, horizontal advection provided forcing for destabilization at the 16-km level almost everywhere inside of the 140-km radius. Outside of this radius near 16 km, however, existed a region of forcing for stabilization. This switch in signs was a consequence of a reversal of the radial gradient of mean N^2 near the 140-km radius (Fig. 3b). Inside of that radius, $(\partial/\partial r)(\partial\theta/\partial z) > 0$ and $u > 0$, which corresponds to forcing for destabilization in Eq. 9; outside of that radius $(\partial/\partial r)(\partial\theta/\partial z) < 0$ and $u > 0$, which corresponds to forcing for stabilization.

The relative importance of the first and third terms on the right-hand side of Eq. 9 is difficult to ascertain, but the structure of the mean radial velocity, θ , and N^2 fields suggests that both terms are contributing within the outflow layer.

Meanwhile in the lower stratosphere, a thin layer of 2-4 m s⁻¹ inflow developed a few hundred meters above the tropopause, similar to that which was observed in Hurricane Patricia (2015; Duran and Molinari 2018). Since the isentropes in this layer slope slightly upward with radius (i.e. $\partial\theta/\partial r < 0$), this inflow acts to import lower θ air to inner radii. There also existed strong radial gradients of mean N^2 in this layer during this time (Fig. 3b), so the inflow layer must have acted to rearrange N^2 . This rearrangement could not have been responsible for the overall increase in N^2 during this period, however. If horizontal advection contributed to the strengthening stable layer just above the tropopause, it must have been through the tilting term. The inflow maximum near the 18-km level represents the level at which the sign of $\partial u/\partial z$ reverses, with $\partial u/\partial z < 0$ below and $\partial u/\partial z > 0$ above. The third term on the right-hand side of Eq. 9 suggests that the tilting of isentropes should act to destabilize the layer below the inflow maximum and stabilize the layer above, and this was observed in Fig. 8a.

281 *b. The role of radiation*

282 During the initial spin-up period (0-24 hours; 9a), convection was not deep enough to deposit
283 large quantities of ice near the tropopause in the mean. Due to the lack of ice particles, the
284 radiative heating tendencies during this period (Fig. 9b) were relatively small and confined to the
285 region above a few particularly strong convective towers. During RI (24-48 hours; Fig. 9b), the
286 eyewall updraft strengthened and a radially-extensive cirrus canopy developed near the tropopause.
287 The enhanced vertical gradient of ice mixing ratio at the top of the cirrus canopy induced strong
288 diurnal-mean radiative cooling near the tropopause (9d). This cooling exceeded 0.6 K h^{-1} in some
289 places and sloped downward from the lower stratosphere into the upper troposphere, following the
290 top of the cirrus canopy. A small radiative warming maximum also appeared outside of the 140-km
291 radius below this region of cooling. These results broadly agree with those of Bu et al. (2014; see
292 their Fig. 11a), whose CM1 simulations 0.3 K net diurnally-averaged radiative cooling at the top
293 of the cirrus canopy and radiative warming within the cloud maximized near the 200-km radius.
294 The broad region of radiative cooling acted to destabilize the layer below the cooling maximum
295 and stabilize the layer above, which can be seen in Fig. 6d. The small area of net radiative heating
296 outside of the 140-km radius enhanced the destabilization in this region and produced a thin layer
297 of stabilization in the 15-16-km layer.

298 After the TC's RI period completed (48-72 hours; Fig. 9f), strong radiative cooling remained
299 near the tropopause at inner radii, sloping downward with the top of the cirrus canopy to below the
300 tropopause at outer radii. Cooling rates exceeded 1 K h^{-1} just above the tropopause between the 30-
301 and 70-km radii. These cooling rates exceeded those observed by Bu et al. (2014), a discrepancy
302 that is likely a consequence of their larger vertical grid spacing (625 m) compared to that used here

(250 m), with a possible a contribution from differing radiation schemes⁵. Time-mean radiative warming spread from 30- to 160-km radius within the cirrus canopy. The existence of radiative cooling overlying radiative warming in this region led to radiatively-forced destabilization at and below the tropopause, as was observed in Fig. 7d. Below the warming layer existed a region of forcing for stabilization, while a much stronger region of forcing for destabilization existed above the cooling maximum in the lower stratosphere.

The results herein suggest that radiative heating tendencies played an important role in destabilizing the upper troposphere and stabilizing the lower stratosphere after the cirrus canopy developed and persisted during and after RI.

c. The role of turbulent mixing

Although vertical turbulence always acts to eliminate vertical gradients of θ , this adjustment toward a neutral state only occurs where the mixing takes place. If turbulence occurs in a stably-stratified layer, it will act to decrease θ at the top of the layer and increase it below. Just above and just below the mixed layer, however, the θ profile remains undisturbed. Consequently, although turbulent mixing acts to decrease $\partial\theta/\partial z$ in the layer in which it is occurring, it actually increases $\partial\theta/\partial z$ just below and just above the layer. These vertical gradients of turbulent mixing are quite important, particularly on the flanks of the upper-tropospheric outflow jet.

Diurnal variability of static stability in the upper troposphere is an interesting area of future research.

⁵Bu et al. (2014) employed the NASA-Goddard radiation scheme for their CM1 simulations, whereas RRTMG is used in the present paper. They did use the RRTMG radiation scheme alongside the Thompson microphysics parameterization for their HWRP simulations, but those simulations also produced smaller radiative tendencies than those seen here (see their Fig. 5a), suggesting that vertical resolution accounts for most of the difference in radiative heating rates.

322 Bu et al. did not see a lower-stratospheric inflow layer, likely due to their 625-m grid spacing.
323 If we want to resolve properly the radiative cooling at the top of the cirrus canopy and the lower-
324 stratospheric inflow layer, we must have sufficient vertical resolution in the tropopause layer. Our
325 100-m grid spacing here may not even be sufficient, given how shallow the layer is! Did my no-
326 CRF simulation show a lower-stratospheric inflow layer?? If not, that's strong evidence supporting
327 the role of radiation in producing the descending inflow layer above the tropopause.

328 *Acknowledgments.* We are indebted to George Bryan for his continued development and support
329 of Cloud Model 1. We also thank Jeffrey Kepert, Robert Fovell, and Erika Navarro for helpful
330 conversations related to this work. This research was supported by NSF Grant #1636799.

331 APPENDIX

332 Sensitivity experiments

333 The simulations exhibited some sensitivity to the initial thermodynamic profile and the prescribed
334 vertical mixing length. Although the details of the intensification and the tropopause-layer N^2 evo-
335 lution varied when these quantities were changed, the conclusions of the paper remain unchanged.

336 *a. Sensitivity to the initial thermodynamic profile*

337 A number of sensitivity experiments were conducted using a variety of initial soundings. Chang-
338 ing the initial temperature and humidity profiles affected the timing of the onset of organized deep
339 convection and the rapidity of intensification. In all simulations, however, convection eventually
340 penetrated to the tropopause, at which time vertical turbulence and radiation combined with ad-
341 vection to adjust the N^2 profile toward that which was observed in the control run. By the end of
342 the RI period in every simulation, all three processes were actively modifying the N^2 profile near
343 the tropopause.

b. Sensitivity to the vertical mixing length

The intensity of parameterized turbulence is highly dependent on a prescribed length scale. Since there is no theoretical or observational guidance for the selection of this mixing length, the value used in the control run (100 m) is based on the sensitivity experiments of Bryan (2012). Since the vertical eddy viscosity varies linearly with the vertical mixing length, prescribing a smaller mixing length produces smaller θ tendencies due to turbulence. Even with a mixing length on the low end of those tested by Bryan (2012), however, turbulence still plays a role in the tropopause-layer N^2 evolution. FIG shows the N^2 evolution in a simulation identical to the control run, except with a vertical mixing length of 50 m rather than 100 m. DESCRIPTION OF THE FIGURE

References

- Bryan, G. H., 2012: Effects of surface exchange coefficients and turbulence length scales on the intensity and structure of numerically simulated hurricanes. *Mon. Wea. Rev.*, **140**, 1125–1143.
- Bryan, G. H., and R. Rotunno, 2009: The maximum intensity of tropical cyclones in axisymmetric numerical model simulations. *Mon. Wea. Rev.*, **137**, 1770–1789.
- Bu, Y. P., R. G. Fovell, and K. L. Corbosiero, 2014: Influence of cloud-radiative forcing on tropical cyclone structure. *J. Atmos. Sci.*, **71**, 1644–1622.
- Doyle, J. D., and Coauthors, 2017: A view of tropical cyclones from above: The Tropical Cyclone Intensity (TCI) Experiment. *Bull. Amer. Meteor. Soc.*, **98**, 2113–2134.
- Duran, P., and J. Molinari, 2018: Dramatic inner-core tropopause variability during the rapid intensification of Hurricane Patricia (2015). *Mon. Wea. Rev.*, **146**, 119–134.

365 Emanuel, K., 2012: Self-stratification of tropical cyclone outflow. Part II: Implications for storm
 366 intensification. *J. Atmos. Sci.*, **69**, 988–996.

367 Emanuel, K., and R. Rotunno, 2011: Self-stratification of tropical cyclone outflow. Part I: Impli-
 368 cations for storm structure. *J. Atmos. Sci.*, **68**, 2236–2249.

369 Iacono, M. J., J. S. Delamere, E. J. Mlawer, M. W. Shephard, S. A. Clough, and W. D. Collins,
 370 2008: Radiative forcing by long-lived greenhouse gases: Calculations with the AER radiative
 371 transfer models. *J. Geophys. Res.*, **113** (D13103).

372 Kepert, J. D., J. Schwendike, and H. Ramsay, 2016: Why is the tropical cyclone boundary layer
 373 not "well mixed"? *J. Atmos. Sci.*, **73**, 957–973.

374 Kimberlain, T. B., E. S. Blake, and J. P. Cangialosi, 2016: Tropical cyclone report: Hurricane
 375 Patricia. National Hurricane Center. [Available online at www.nhc.noaa.gov].

376 Komaromi, W. A., and J. D. Doyle, 2017: Tropical cyclone outflow and warm core structure as
 377 revealed by HS3 dropsonde data. *Mon. Wea. Rev.*, **145**, 1339–1359.

378 Markowski, P. M., and G. H. Bryan, 2016: LES of laminar flow in the PBL: A potential problem
 379 for convective storm simulations. *Mon. Wea. Rev.*, **144**, 1841–1850.

380 Ohno, T., and M. Satoh, 2015: On the warm core of a tropical cyclone formed near the tropopause.
 381 *J. Atmos. Sci.*, **72**, 551–571.

382 Rogers, R. F., S. Aberson, M. M. Bell, D. J. Cecil, J. D. Doyle, J. Morgerman, L. K. Shay, and
 383 C. Velden, 2017: Re-writing the tropical record books: The extraordinary intensification of
 384 Hurricane Patricia (2015). *Bull. Amer. Meteor. Soc.*, **98**, 2091–2112.

385 Rotunno, R., and K. A. Emanuel, 1987: An air-sea interaction theory for tropical cyclones. Part II:
386 Evolutionary study using a nonhydrostatic axisymmetric numerical model. *J. Atmos. Sci.*, **44**,
387 542–561.

388 Stern, D. P., and F. Zhang, 2013: How does the eye warm? Part I: A potential temperature budget
389 analysis of an idealized tropical cyclone. *J. Atmos. Sci.*, **70**, 73–89.

390 Thompson, G., R. M. Rasmussen, and K. Manning, 2004: Explicit forecasts of winter precipitation
391 using an improved bulk microphysics scheme. Part I: Description and sensitivity analysis. *Mon.*
392 *Wea. Rev.*, **132**, 519–542.

393 LIST OF FIGURES

394	Fig. 1.	The maximum 10-m wind speed (top panel; m s^{-1}) and minimum sea-level pressure (bottom	
395		panel; hPa) in the simulated storm (blue lines) and from Hurricane Patricia's best track (red	
396		stars).	23
397	Fig. 2.	Left panels: Twenty-four-hour changes in squared Brunt-Väisälä frequency (N^2 ; 10^{-4} s^{-2})	
398		over (top row) 0-24 hours, (middle row) 24-48 hours, (bottom row) 48-72 hours. Middle	
399		Panels: The N^2 change over the same time periods computed using Eqs. 4-6, Right Panels:	
400		The budget residual over the same time periods, computed by subtracting the budget change	
401		(middle column) from the model change (left column).	24
402	Fig. 3.	Twenty-four-hour averages of squared Brunt-Väisälä frequency (N^2 ; 10^{-4} s^{-2}) over (a) 0-24	
403		hours, (b) 24-48 hours, (c) 48-72 hours. Orange lines represent the cold-point tropopause	
404		averaged over the same time periods.	25
405	Fig. 4.	Time series of the contribution of each of the budget terms to the time tendency of the	
406		squared Brunt-Väisälä frequency (N^2 ; 10^{-4} s^{-2}). For each budget term, the absolute value	
407		of the N^2 tendency is averaged temporally over 1-hour periods (using output every minute),	
408		and spatially in a region extending from 0 to 200 km radius and 14 to 21 km altitude.	26
409	Fig. 5.	(a) Total change in N^2 over the 0-24-hour period ($10^{-4} \text{ s}^{-2} (24 \text{ h})^{-1}$) and the contributions to	
410		that change from (b) the sum of horizontal and vertical advection, (c) vertical turbulence, (d)	
411		longwave and shortwave radiation, (e) the sum of horizontal advection, vertical advection,	
412		and vertical turbulence, and (f) the sum of horizontal advection, vertical advection, vertical	
413		turbulence, and longwave and shortwave radiation.	27

414	Fig. 6.	As in Fig. 5, but for the 24-48-hour period.	28
415	Fig. 7.	As in Fig. 5, but for the 48-72-hour period.	29
416	Fig. 8.	The contribution to the change in N^2 over the 24-48-hour period ($10^{-4} \text{ s}^{-2} (24 \text{ h})^{-1}$) by (a) hor-	
417		izontal advection and (b) vertical advection. (c) The radial velocity (m s^{-1} ; filled contours),	
418		potential temperature (K; thick black contours), cold-point tropopause height (orange line),	
419		and level of maximum outflow (dashed cyan line) averaged over the 24-48-hour period. (d)	
420		The vertical velocity (cm s^{-1} ; filled contours), potential temperature (K; thick black con-	
421		tours), and cold-point tropopause height (orange line) averaged over the 24-48-hour period.	
422		30	
423	Fig. 9.	Ice mixing ratio (g kg^{-1}) and cold-point tropopause height (orange lines) averaged over (a)	
424		0-24 hours, (c) 24-48 hours, and (e) 48-72 hours. Radiative heating rate (K h^{-1}) and cold-	
425		point tropopause height (orange lines) averaged over (b) 0-24 hours, (d) 24-48 hours, and (f)	
426		48-72 hours.	31
427	Fig. 10.	Vertical eddy diffusivity ($\text{m}^2 \text{ s}^{-2}$; filled contours), cold-point tropopause height (cyan lines),	
428		and radial velocity (m s^{-1} ; thick black lines) averaged over (a) 0-24 hours, (b) 24-48 hours,	
429		and (c) 48-72 hours.	32

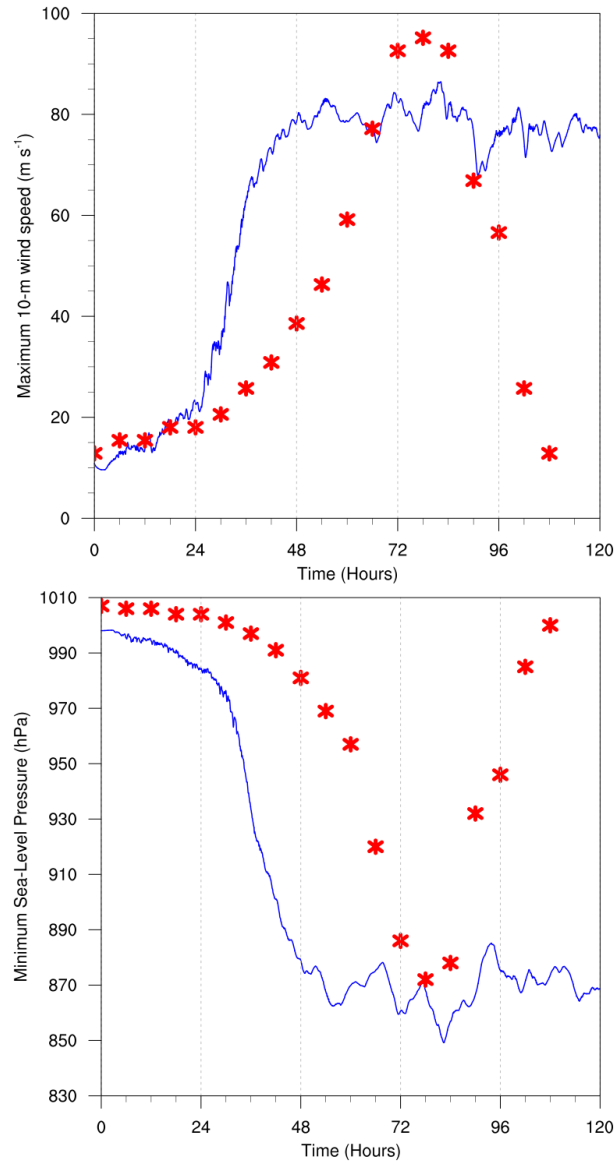


FIG. 1. The maximum 10-m wind speed (top panel; m s^{-1}) and minimum sea-level pressure (bottom panel; hPa) in the simulated storm (blue lines) and from Hurricane Patricia's best track (red stars).

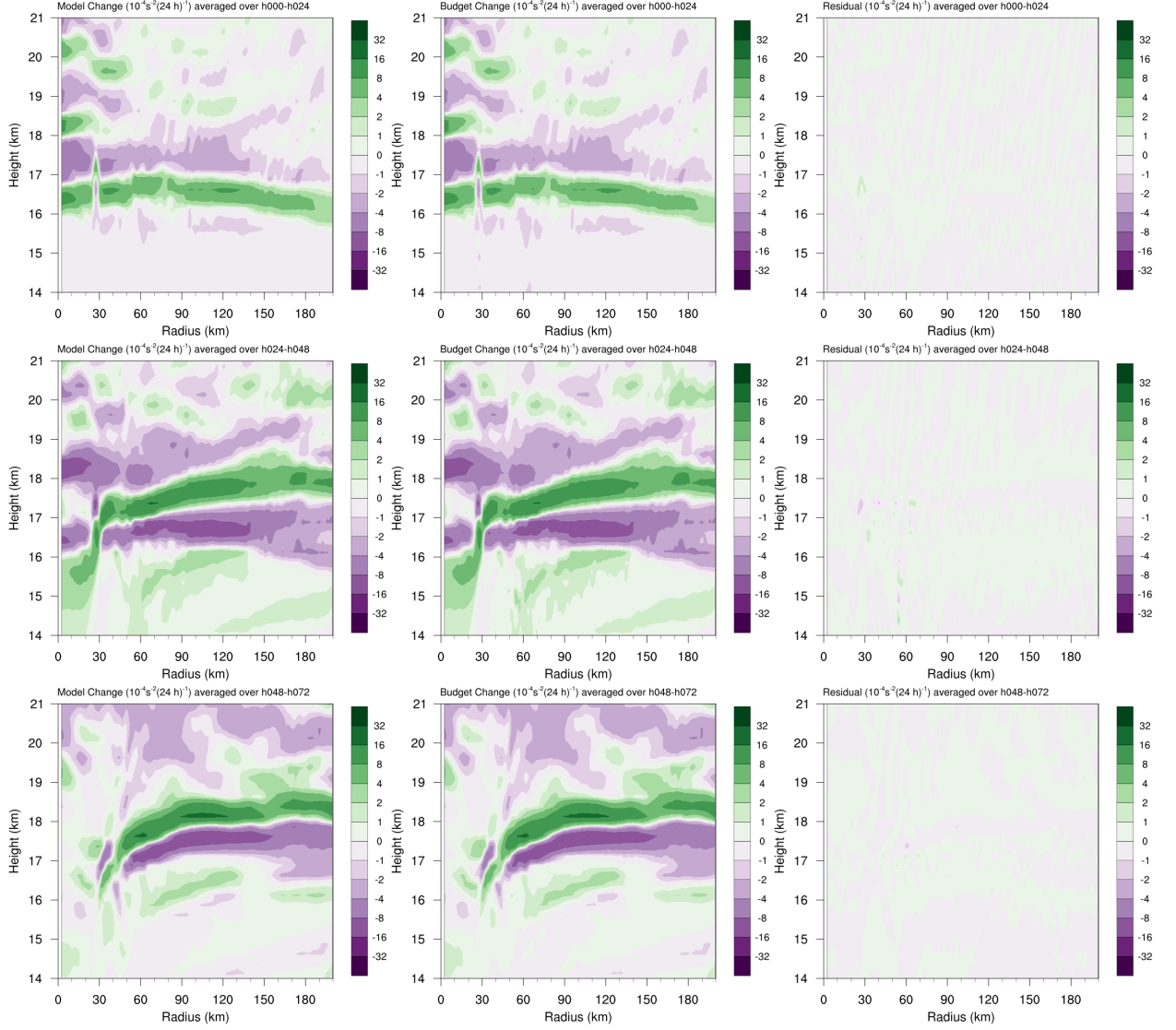
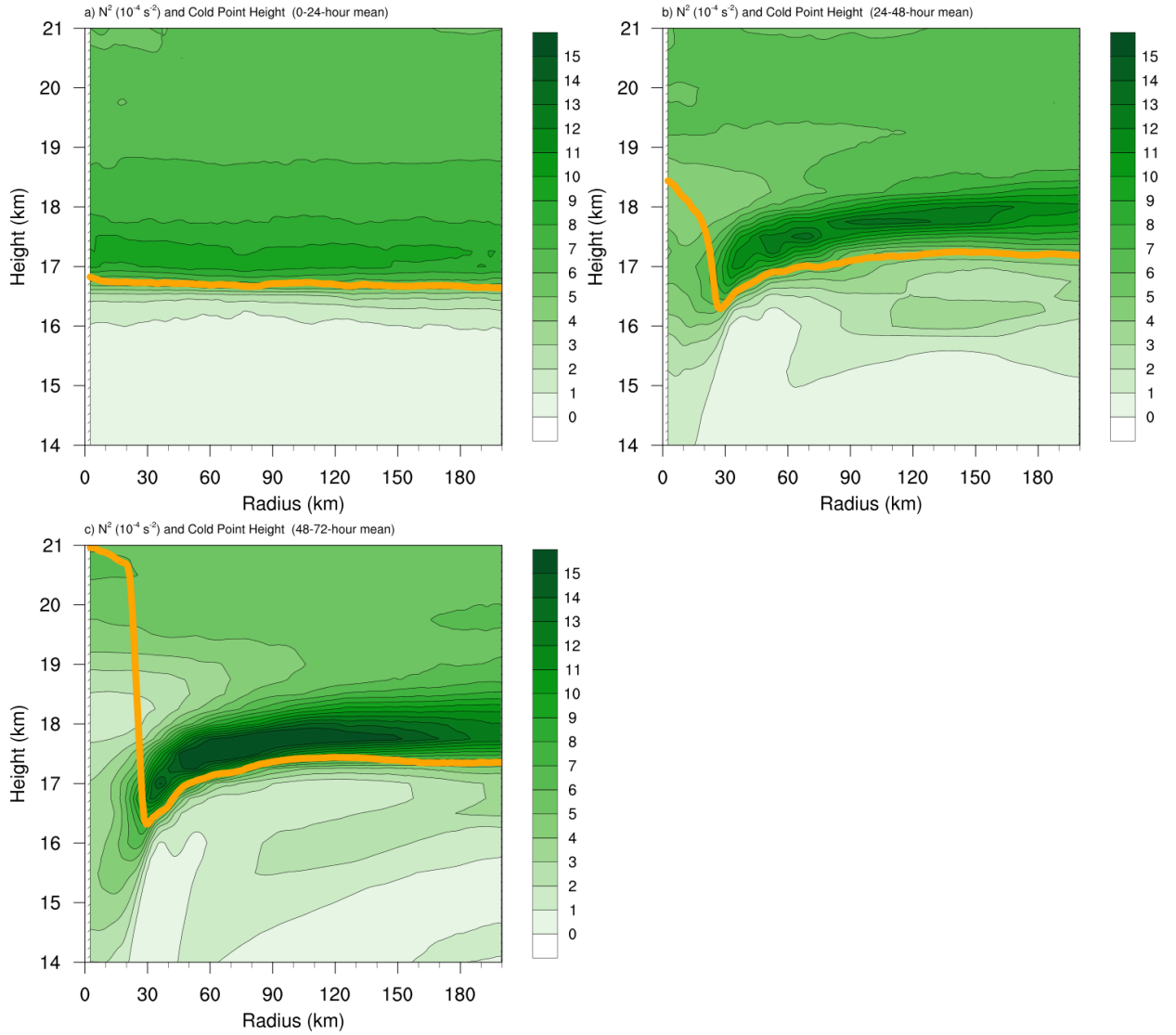


FIG. 2. Left panels: Twenty-four-hour changes in squared Brunt-Väisälä frequency (N^2 ; 10^{-4} s^{-2}) over (top row) 0-24 hours, (middle row) 24-48 hours, (bottom row) 48-72 hours. Middle Panels: The N^2 change over the same time periods computed using Eqs. 4-6, Right Panels: The budget residual over the same time periods, computed by subtracting the budget change (middle column) from the model change (left column).



436 FIG. 3. Twenty-four-hour averages of squared Brunt-Väisälä frequency (N^2 ; 10^{-4} s^{-2}) over (a) 0-24 hours,
 437 (b) 24-48 hours, (c) 48-72 hours. Orange lines represent the cold-point tropopause averaged over the same time
 438 periods.

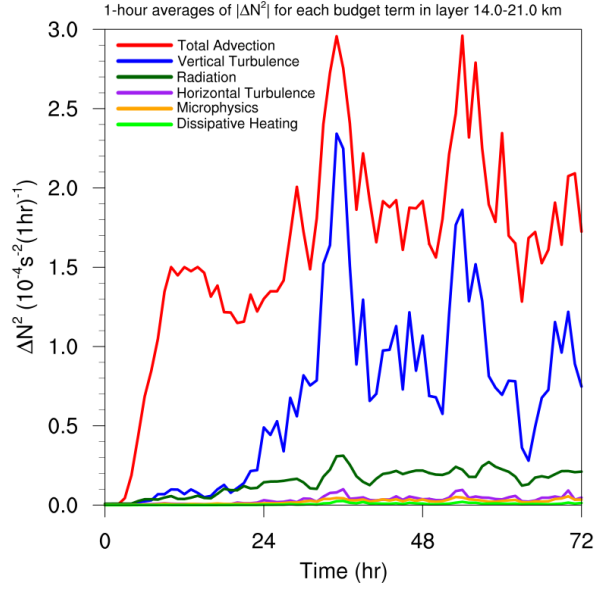
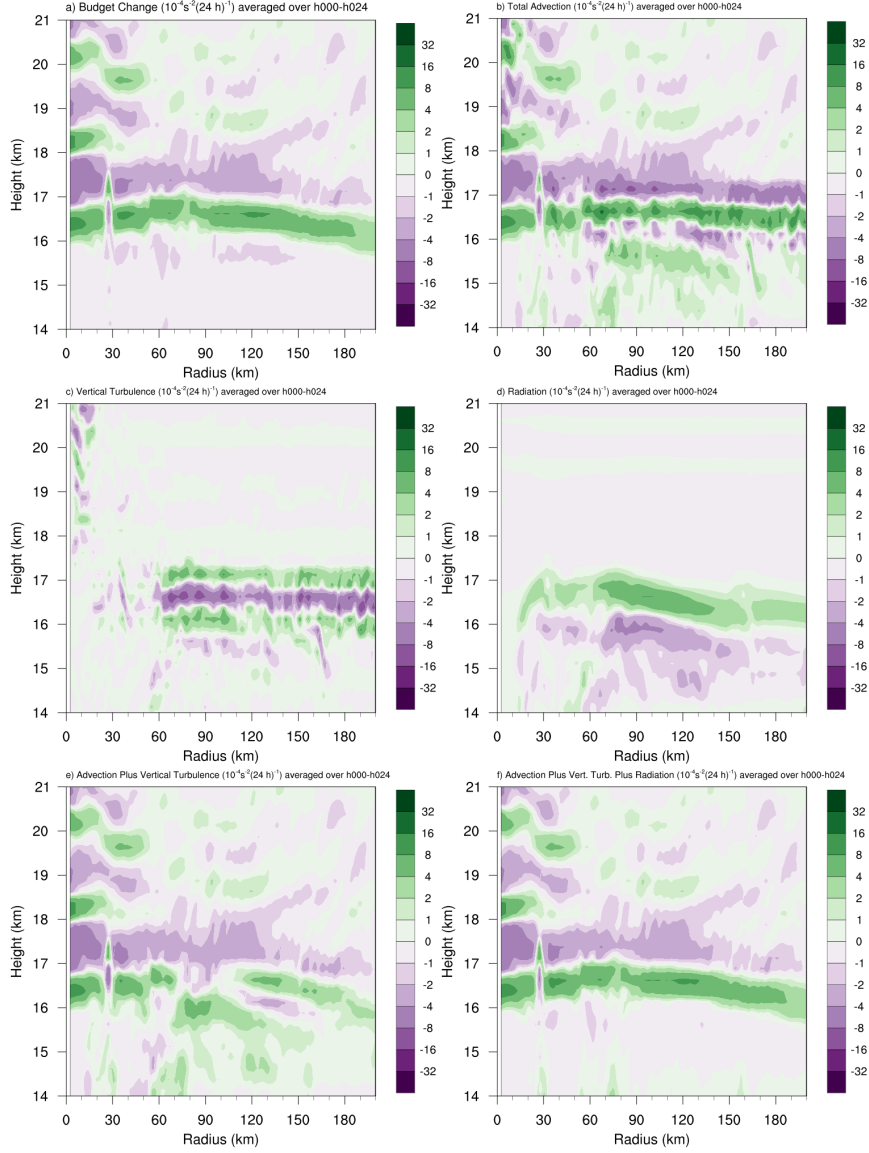


FIG. 4. Time series of the contribution of each of the budget terms to the time tendency of the squared Brunt-Väisälä frequency (N^2 ; 10^{-4} s^{-2}). For each budget term, the absolute value of the N^2 tendency is averaged temporally over 1-hour periods (using output every minute), and spatially in a region extending from 0 to 200 km radius and 14 to 21 km altitude.



443 FIG. 5. (a) Total change in N^2 over the 0-24-hour period ($10^{-4} \text{ s}^{-2} (24 \text{ h})^{-1}$) and the contributions to that change
 444 from (b) the sum of horizontal and vertical advection, (c) vertical turbulence, (d) longwave and shortwave
 445 radiation, (e) the sum of horizontal advection, vertical advection, and vertical turbulence, and (f) the sum of
 446 horizontal advection, vertical advection, vertical turbulence, and longwave and shortwave radiation.

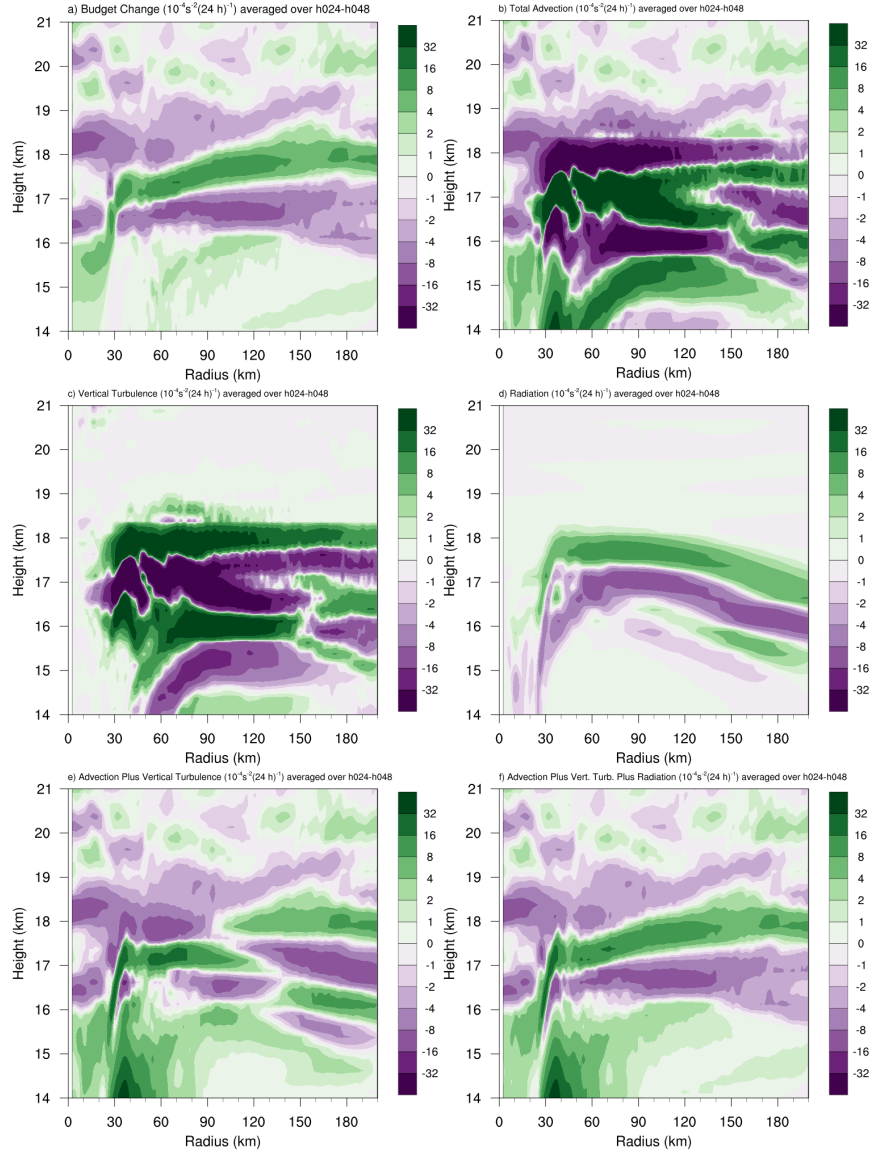


FIG. 6. As in Fig. 5, but for the 24-48-hour period.

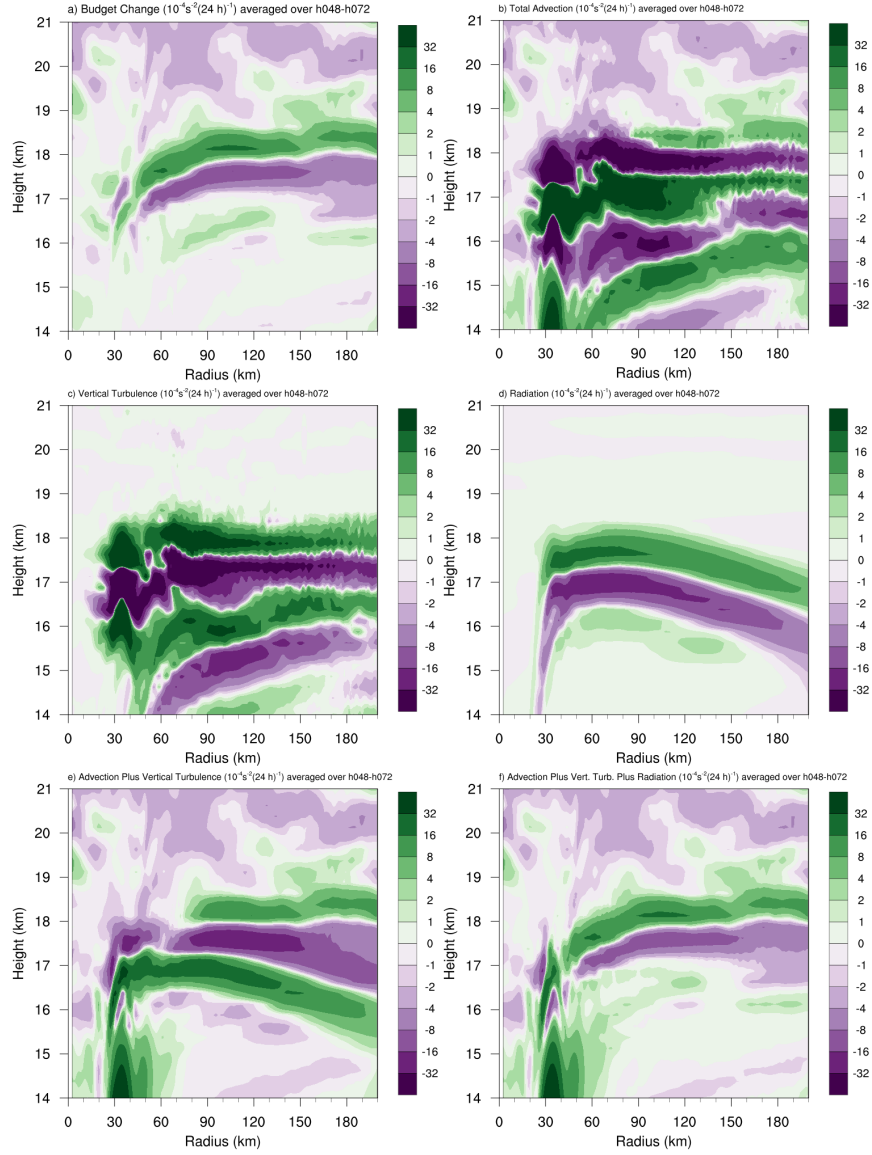


FIG. 7. As in Fig. 5, but for the 48-72-hour period.

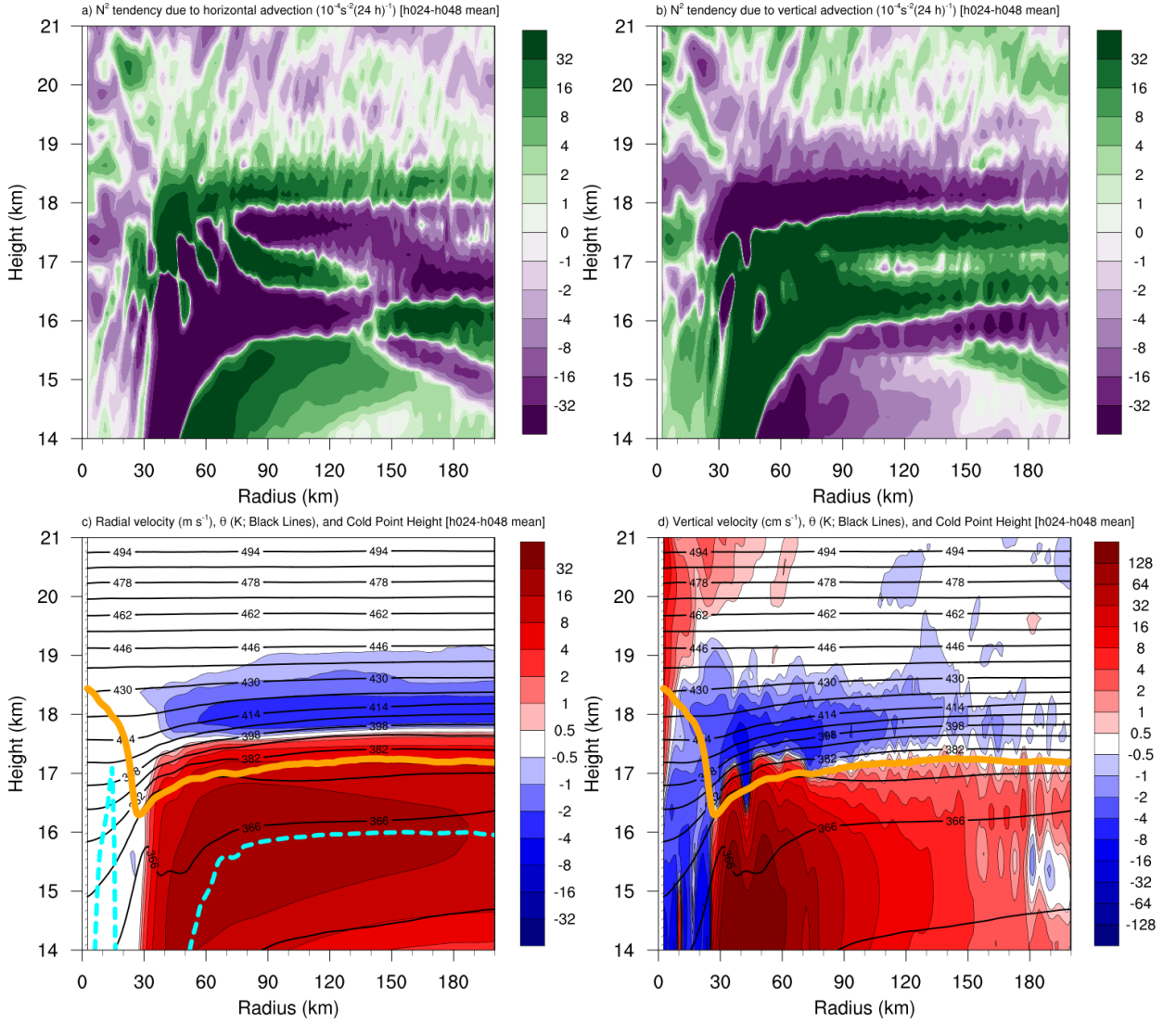
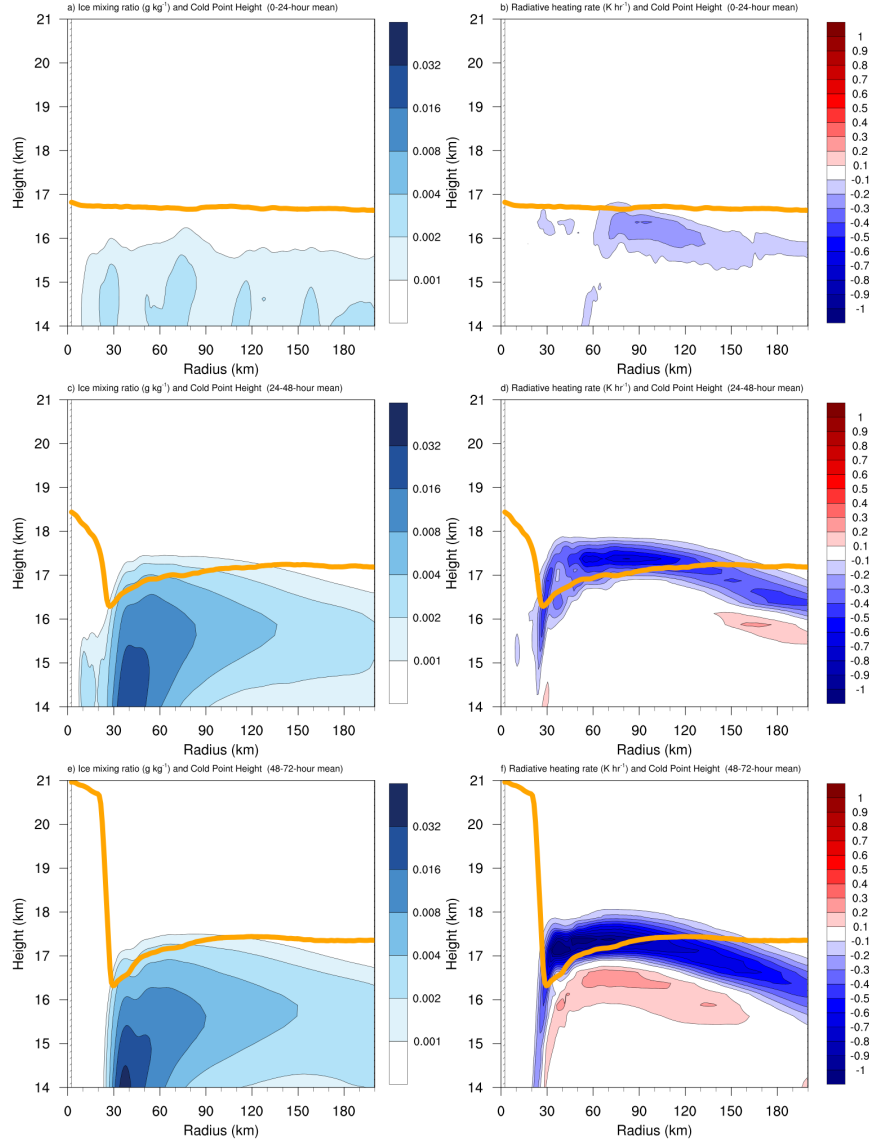


FIG. 8. The contribution to the change in N^2 over the 24-48-hour period ($10^{-4} \text{s}^{-2} (24 \text{ h})^{-1}$) by (a) horizontal advection and (b) vertical advection. (c) The radial velocity (m s^{-1} ; filled contours), potential temperature (K; thick black contours), cold-point tropopause height (orange line), and level of maximum outflow (dashed cyan line) averaged over the 24-48-hour period. (d) The vertical velocity (cm s^{-1} ; filled contours), potential temperature (K; thick black contours), and cold-point tropopause height (orange line) averaged over the 24-48-hour period.



453 FIG. 9. Ice mixing ratio (g kg^{-1}) and cold-point tropopause height (orange lines) averaged over (a) 0-24 hours,
 454 (c) 24-48 hours, and (e) 48-72 hours. Radiative heating rate (K h^{-1}) and cold-point tropopause height (orange
 455 lines) averaged over (b) 0-24 hours, (d) 24-48 hours, and (f) 48-72 hours.

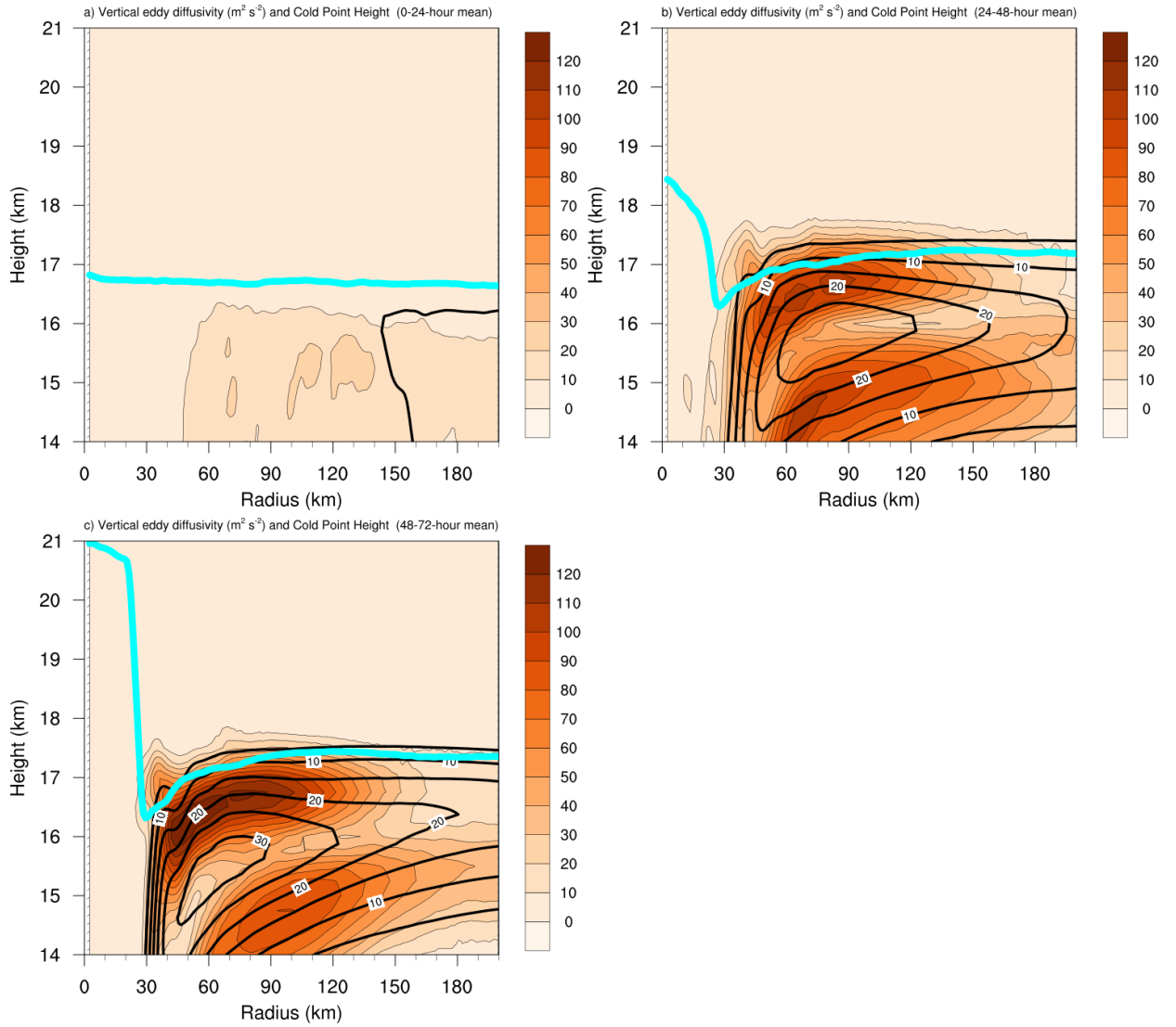


FIG. 10. Vertical eddy diffusivity ($\text{m}^2 \text{s}^{-2}$; filled contours), cold-point tropopause height (cyan lines), and radial velocity (m s^{-1} ; thick black lines) averaged over (a) 0-24 hours, (b) 24-48 hours, and (c) 48-72 hours.